Supporting information

Catalytic consequences of Pt particle size and chloride promotion in the ring opening of cyclopentane on Pt/Al_2O_3

*Hui Shi[a], Oliver Y. Gutiérrez[a], Hao Yang[b], Nigel D. Browning[c], Gary L. Haller[a], Johannes A. Lercher[a,]**

[a] *Department of Chemistry and Catalysis Research Center, Technische Universität München, Lichtenbergstraße 4, D-85747 Garching, Germany*

[b] *Department of Chemical Engineering and Materials Science, University of California-Davis, One Shields Avenue, Davis, CA 95616, USA*

[c] *Fundamental and Computational Sciences Directorate, Pacific Northwest National Laboratory, Richland, WA 99352, USA*

* Corresponding author: johannes.lercher@ch.tum.de (J.A. Lercher)

Fax: +49 89 28913544; Tel: +49 89 28913540.

S1. CO adsorption experiments on high-dispersion Pt catalysts prepared from Cl-free and Cl-containing precursors

S1.1. Experimental

The infrared spectra of adsorbed CO were monitored in transmission mode on a Bruker VERTEX 70 spectrometer at a resolution of 4 cm^{-1}. The samples were prepared as self-supporting wafers (10−12 mg cm^{-2}) and activated in static H_2 (p = 15 ± 3 mbar) for 2 h at 673 K (heating rate = 10 K min^{-1}). After cooling to 313−318 K, the samples were exposed to successive doses of CO (p = 2.0×10^{-6}–1.0×10^{-1} mbar), equilibrated at each pressure for ca. 5 min and then outgassed (p = 2.0−3.5×10^{-7} mbar) for ca. 20 min. All spectra were collected at 318 ± 3 K. Infrared absorption bands in 1990−2200 cm^{-1} were fitted with combined Gaussian and Lorentz functions for quantitative deconvolution of overlapping peaks.

S1.2. Results

The infrared frequency shift of CO* on different surface structures or in the presence of different electronic promoters is usually attributed to electron availability in the metal particle to participate in backbonding to the anti-bonding orbitals of chemisorbed CO, though such shifts can be complicated by coverage effects [S1−S4].

Infrared spectra for Pt(0.88)-2/Al_2O_3, Pt(0.71)-2/Al_2O_3, and Pt(0.81)-1/Al_2O_3 samples equilibrated with CO (3.7−4.5×10^{-4} mbar, 318 ± 3 K), corresponding to 8−11% of saturation monolayer CO* coverage, are shown in Fig. S4 (solid thick lines). The saturation of Pt surface with CO* occurs on all these samples at pressures higher than 1.0×10^{-2} mbar. The dosing pressure and corresponding CO* coverage was chosen as a compromise between acceptable signal intensities and low CO* coverage to minimize the dipole coupling effects.

The band at 2070-2090 cm^{-1} has been assigned to linear on-top CO* [S1−S7]. The peaks from the reduced catalysts, however, featured low-frequency inhomogeneous line broadening in addition to a distinct high-frequency shoulder. Infrared CO absorption peaks with a similar shape were also shown by Greenler and co-workers [S5,S6] and Fanson et al. [S7]. There can be many factors contributing to the observed shape of CO adsorption bands on these catalysts, such as a relatively broad particle size distribution, or intensity transfer due to dipole coupling [S1]. While these factors may have their impacts

on the wavenumbers and intensity ratios between different peaks resolved from the adsorption band, we believe that the very similar average particle sizes (1.1−1.4 nm) and similarly low CO* coverages among these catalysts render the comparison of electronic states of Pt on the basis of CO-stretching vibrational frequencies/wavenumbers essentially valid for these spectra.

The deconvoluted peaks (thin lines) and the related wavenumbers were shown in Fig. S4. Sums of three peak components gave good fits to the measured spectra. The full widths at half-maximum (FWHM) increased with decreasing wavenumbers for different peaks. Irrespective of the Cl contents in the catalyst, the three peaks appeared at 2083−2089, 2069−2070, 2033−2035 cm^{-1}. The FWHM for these peaks were 65−68, 29−30 and 11−12 cm^{-1}, respectively. Greenler and coworkers determined that the high-, medium-, and low-frequency components were due to crystallite facet faces, corners, and edges, respectively [S6]. More generally, the lines shifted to higher wavenumbers with the increasing coordination number of surface sites [S5]. Regardless, Fig. S4 shows that the CO stretching frequencies failed to discriminate the difference in the electron density of surface Pt atoms in these catalysts with similar particle sizes but were prepared from Cl-free or Cl-containing precursors.

S2. Validation of the assumption that dependence of benzene hydrogenation rates on H_2 pressure does not differ in the absence and the presence of toluene

In a pure benzene feed, the rate for benzene hydrogenation (R_B^0) is given by:

$$R_B^0 = f^0(H_2)k_BK_BP_B/(1 + K_BP_B) \quad \text{(S1)}$$

in which k_B and K_B are the rate constant of the rate-determining step for benzene hydrogenation and the equilibrium constant for the adsorption of benzene, respectively.

In a mixture of benzene and toluene with partial pressures P_B and P_T, the rate of benzene hydrogenation (R_B) is given by:

$$R_B = f(H_2)k_BK_BP_B/(1 + K_BP_B + K_TP_T) \quad \text{(S2)}$$

in which k_B, K_B and K_T are the rate constant of the rate-determining step for benzene hydrogenation, the equilibrium constants for the adsorption of benzene (B) and toluene (T), respectively.

If the H_2 pressure dependence is identical in both cases, i.e., $f^0(H_2) = f(H_2)$, and the adsorption sites for aromatics are fully covered ($K_BP_B >> 1$ and $K_BP_B+K_TP_T >> 1$), then

$$R_B^0/R_B = 1 + K_{T/B}(P_T/P_B) \quad \text{(S3)}$$

where $K_{T/B}$ represents the ratio of adsorption coefficient of toluene over that of benzene on a specific catalyst. For the competitive hydrogenation of benzene and toluene in mixtures of these two, the reaction orders in H_2 were found to be very close to those measured in the hydrogenation of pure benzene (inset of Fig. S5), validating the assumption of $f^0(H_2) = f(H_2)$.

S3. Effect of H-adsorption strength on the reaction orders in CP and H_2

We show in this section why we saw a difference in the H_2 reaction order (-1.1 to -1.6 vs. -1.6 to -1.8) on Pt/Al_2O_3 catalysts prepared from Cl-free or Cl-containing precursors (Fig. 3), but not an appreciable difference in the CP reaction order between these two series of catalysts (Fig. 4a).

It is generally accepted that hydrogenolysis of alkanes or cycloalkanes proceeds via dehydrogenated intermediates [S8−S13]. If the active site consists of a pair of unoccupied surface Pt atoms (*-*), and if the prevalent active intermediate is such that four H atoms are abstracted from the C−C bond that is bound to a pair of surface Pt atoms, then

$$c\text{-}C_5H_{10}\,(g) + {}^*\text{-}^* \rightleftharpoons (c\text{-}C_5H_6)^{*\text{-}*} + 2H_2\,(g) \quad \text{(S4)}$$

For H_2 adsorption, we have

$$H_2\,(g) + {}^*\text{-}^* \rightleftharpoons (H)^*\text{-}(H)^* \quad \text{(S5)}$$

By considering site conservation and competitive adsorption for both reactants ($\theta_H + \theta_{cyc} + \theta_v = 1$), the surface coverages by CP-derived species and H* can be expressed as (Eqs. S6 and S7, respectively)

$$\theta_C = \frac{\dfrac{K_{cyc}P_{c-C_5H_{10}}}{P_H^{\,2}}}{1+\dfrac{K_{cyc}P_{c-C_5H_{10}}}{P_H^{\,2}}+K_HP_H} \quad \text{(S6)}$$

$$\theta_H = \frac{K_HP_H}{1+\dfrac{K_{cyc}P_{c-C_5H_{10}}}{P_H^{\,2}}+K_HP_H} \quad \text{(S7)}$$

where K_{cyc} and K_H are the equilibrium constants for (S4) and (S5), respectively.

Instead of fitting the kinetic data with these equations, we started with assumed values for K_{cyc} and K_H and the following considerations, in order to produce good agreement between the predicted and the measured reaction orders under the relevant conditions. First, from the CP reaction order (ca. 0.6), the vacant site cannot be dominant over the other two terms (CP-derived species and H*). Second, a decrease in the H-adsorption strength (a smaller K_H) leads to a less negative reaction order in H_2, and a less pronounced decrease in the CP reaction order. As shown in Fig. S6, when the H-adsorption strength becomes weaker by 25% on the catalyst, the reaction order in H_2 becomes less negative by 0.2, while the reaction order in CP only decreases by 0.06, indicating an increase in coverage by CP-derived intermediates, falling within the uncertainty (± 0.07) of kinetic measurements.

S4. Adsorption stoichiometry of H/Pt$_s$ and its consequence to the reported values of dispersion and TOFs in this study

The dependence of turnover rates for cyclopentane disappearance on corrected Pt dispersion was plotted in Fig. S7, assuming that the adsorption stoichiometry of H/Pt$_s$ linearly decreased from 1.5 on the smallest studied average particle size (D = 0.98 according to the H/Pt$_s$ =1 stoichiometry) to 1.0 on the largest studied particle size (D = 0.07). The dispersion range changed from 0.07-0.98 to 0.07-0.66, and the TOF values changed accordingly. The relevant fact for this work is that, assuming a varying H/Pt$_s$ stoichiometry produces the same type of structure sensitivity, and therefore does not lead to interpretations or conclusions different to those reported in the manuscript. Moreover, evidence from STEM measurements favors the adsorption stoichiometry adopted in the main text (Table 1).

S5. NH_3-TPD experiments

S5.1. Experimental

Temperature-programed desorption of ammonia was performed under flow conditions. The catalysts were activated in helium at 473 K for 1 h using a heating rate of 10 K min^{-1} from room temperature. Ammonia was adsorbed by adding 10 vol.% to the He carrier gas

(total flow 30 ml min^{-1}) at 373 K. The sample was purged with He for 2 h at 373 K in order to remove physisorbed molecules. The sample was heated in flowing He at a rate of 10 K min^{-1} from 373 K to 1043 K for ammonia desorption. The species desorbing were monitored by mass spectrometry (Balzers QME 200). For quantification a standard with known acid site concentration (HZSM-5 with a Si/Al ratio of 45 and acid concentration of 360 μmol g^{-1}) was used.

S5.2. Results

NH_3-TPD curves are shown in Fig. S10. The desorption peak at the higher temperature (ca. 814 K) is ascribed to NH_3 adsorbed on the Lewis-acidic cations (e.g., Al^{3+}), while NH_3 desorbed at a lower temperature (ca. 487 K) should stem from Brønsted acid sites (hydroxyl groups with or without inductive effects of Cl). The total acidities are quantified to be 102, 122, 138 μmol g^{-1} for Pt(0.81)-1/Al_2O_3, Pt(0.88)-2/Al_2O_3 and Pt(0.98)-1/Al_2O_3, respectively. In comparison, the Cl-doped Pt(0.81)-1/Al_2O_3 showed a total acidity of 118 μmol g^{-1}. The Brønsted acidity also scales in a similar fashion among these catalysts.

References

[S1] S.G. Fox, V.M. Browne, P. Hollins, J. Electron Spectrosc. Relat. Phenom. 54/55 (1990) 749.

[S2] A. Crossley, D.A. King, Surf. Sci. 68 (1977) 528.

[S3] P. Hollins, Surf. Sci. Rep. 16 (1992) 51.

[S4] A.D. Allian, K. Takanabe, K.L. Fujdala, X. Hao, T.J. Truex, J. Cai, C. Buda, M. Neurock, E. Iglesia, J. Am. Chem. Soc. 133 (2010) 4498.

[S5] R.K. Brandt, M.R. Hughes, L.P. Bourget, K. Truszkowska, R.G. Greenler, Surf. Sci. 286 (1993) 15.

[S6] R.G. Greenler, K.D. Burch, K. Kretzschmar, R. Klauser, A.M. Bradshaw, B.E. Hayden, Surf. Sci. 152/153 (1985) 338.

[S7] P.T. Fanson, W. N. Delgass, J. Lauterbach, J. Catal. 204 (2001) 35.

[S8] G.C. Bond, Metal-Catalysed Reactions of Hydrocarbons, Springer, Berlin, 2005.

[S9] S.B. Shang, C.N. Kenney, J. Catal. 134 (1992) 134.

[S10] J.H. Sinfelt, D.J.C. Yates, J. Catal. 8 (1967) 82.

[S11] D.J.C. Yates, J.H. Sinfelt, W.F. Taylor, J. Am. Chem. Soc. 86 (1964) 2996.

[S12] A. Cimino, M. Boudart, H. Taylor, J. Phys. Chem. 58 (1954) 796.

[S13] Z.-J. Zhao, L.V. Moskaleva, N. Rösch, J. Catal. 285 (2012) 124.

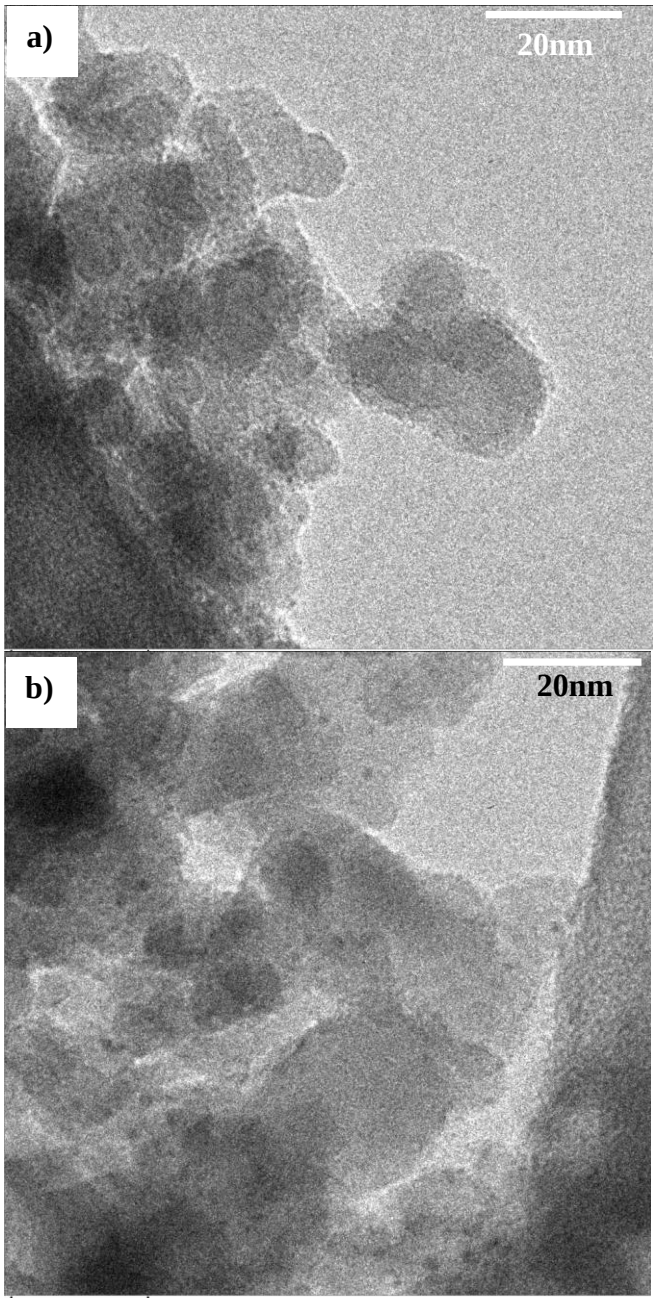
a)
20nm
b)
20nm

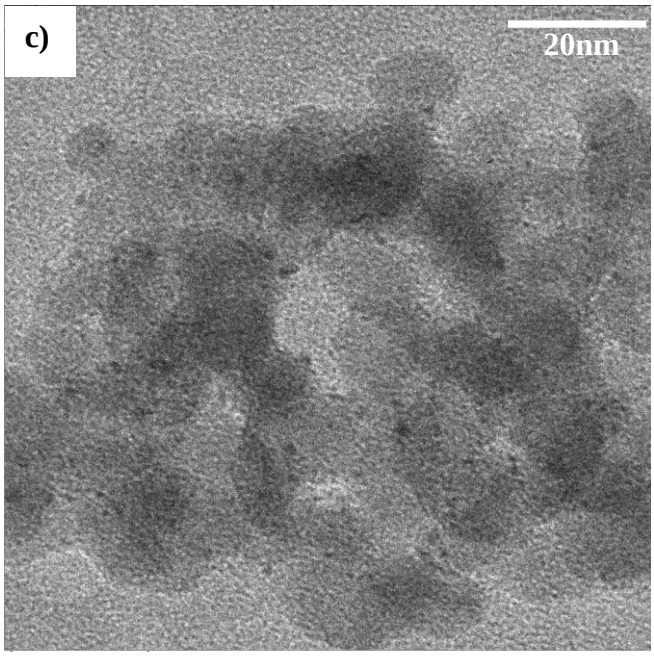
c)
20nm

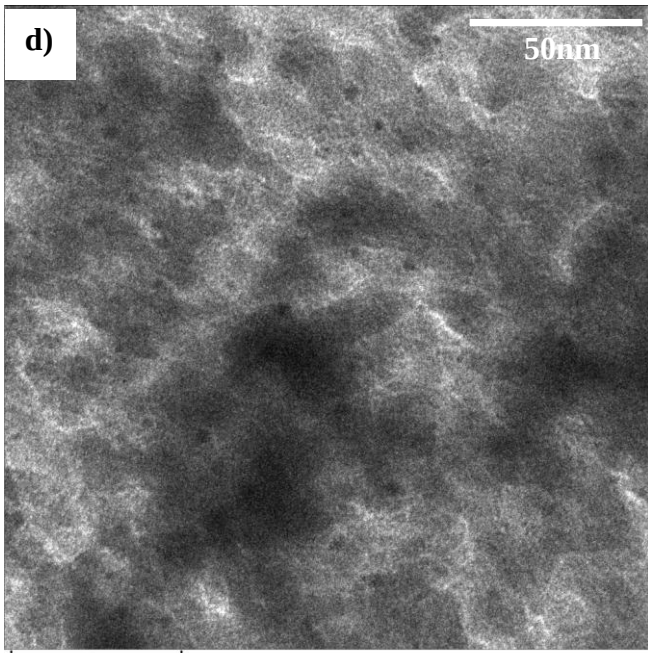
d)
50nm

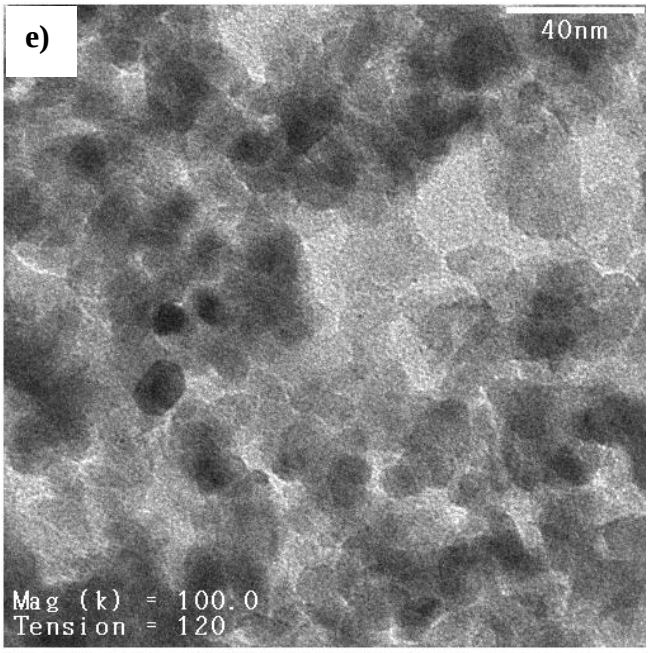
e)
40nm
Mag (k) = 100.0
Tension = 120

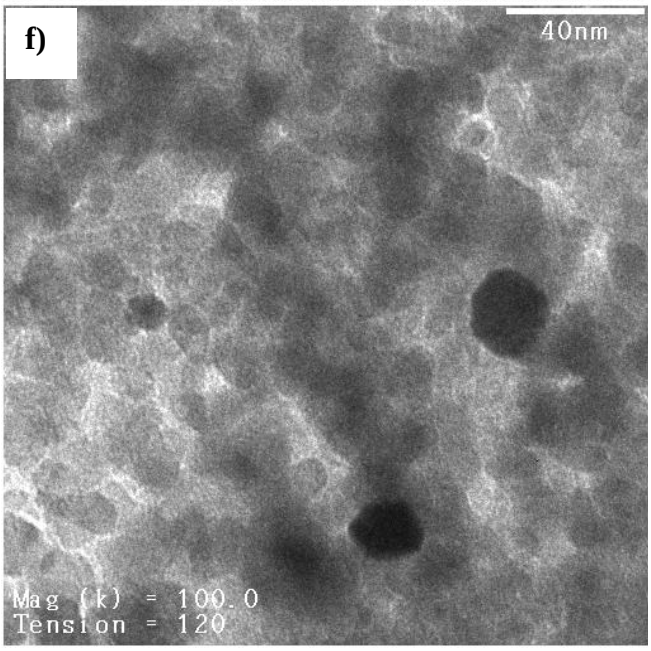
f)
40nm
Mag (k) = 100.0
Tension = 120

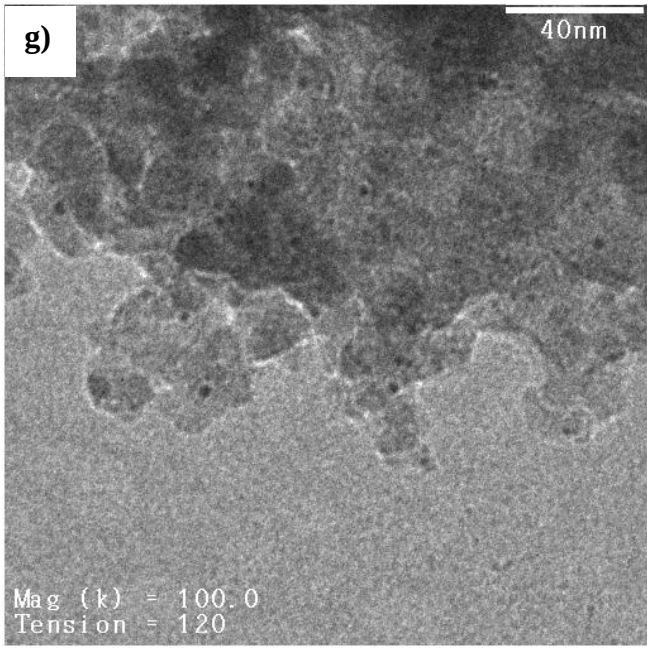

Figure S1. Representative transmission electron microscopy images of (a) 1.05%Pt(0.98)-2/Al_2O_3, (b) 0.96%Pt(0.81)-1/Al_2O_3, (c) 1.07%Pt(0.71)-2/Al_2O_3, (d) 0.98%Pt(0.59)-1/Al_2O_3, (e) 1.10%Pt(0.09)-2/Al_2O_3, (f) 1.00%Pt(0.07)-1/Al_2O_3, and (g) 0.41%Pt(0.55)-1/SiO_2. The corresponding TEM-derived dispersions for (d) to (g): 0.40, 0.08, 0.07 and 0.44.

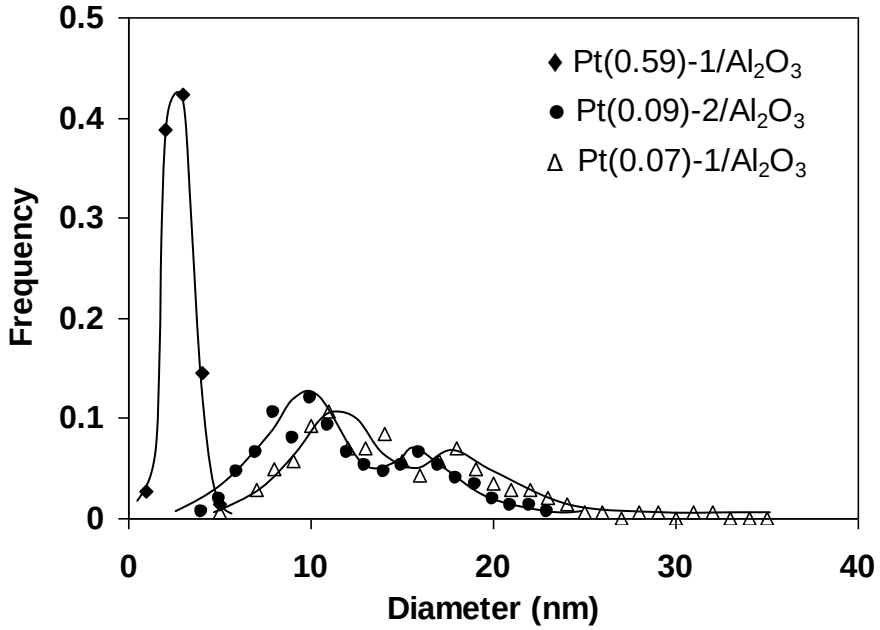

Figure S2. Particle size distribution as determined from an analysis of transmission electron microscopy images for (■) Pt(0.59)-1/Al_2O_3, (●) Pt(0.09)-2/Al_2O_3, (Δ) Pt(0.07)-1/Al_2O_3. Bin size is 0.5 nm, and 140−250 particles were sampled from at least six areas in every case.

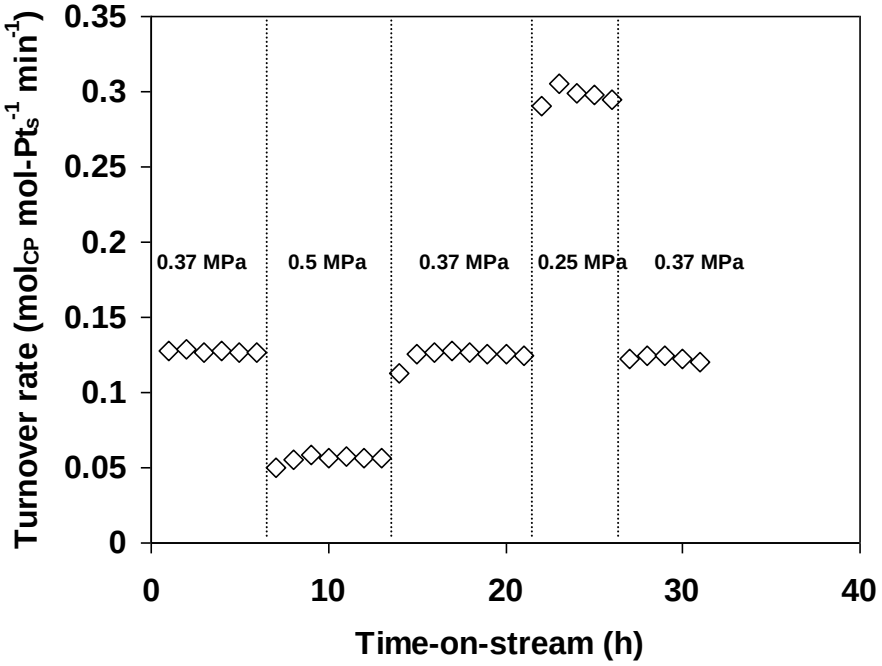

Figure S3. Time-on-stream (TOS) behavior of the 0.98%Pt(0.59)-1/Al_2O_3 catalyst and its responsive behavior to (de)pressurization. Reaction conditions: 533 K, 8.8 kPa CP, and indicated H_2 pressures.

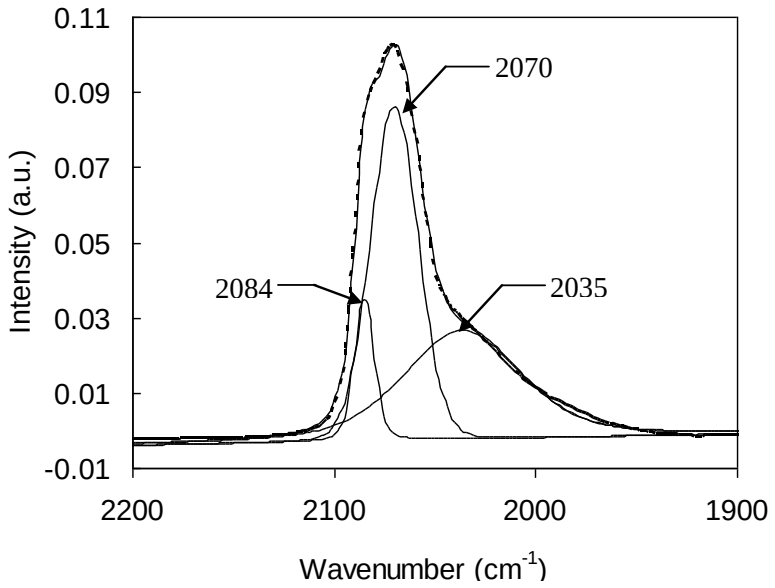
0.11
0.09
0.07
0.05
0.03
0.01
-0.01
Intensity (a.u.)
2070
2084
2035
2200
2100
2000
1900
Wavenumber (cm-1)

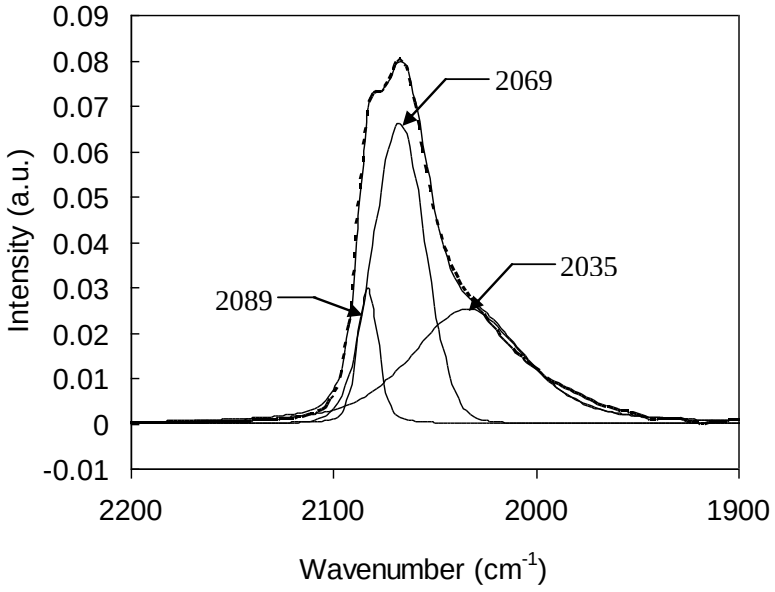
0.09
0.08
0.07
0.06
0.05
0.04
0.03
0.02
0.01
0
-0.01
Intensity (a.u.)
2069
2089
2035
2200
2100
2000
1900
Wavenumber (cm-1)

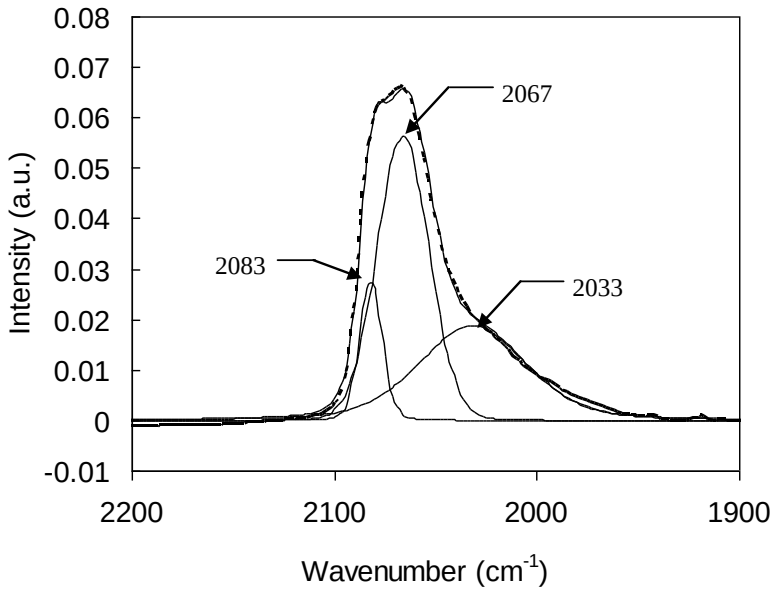

Figure S4. Infrared spectra of CO chemisorbed at 318 (± 3) K for catalysts prepared from hexachloroplatnic acid: (a) Pt(0.88)-2/Al_2O_3, (b) Pt(0.71)-2/Al_2O_3, and one prepared from tetraamine platinum nitrate: (c) Pt(0.81)-1/Al_2O_3.

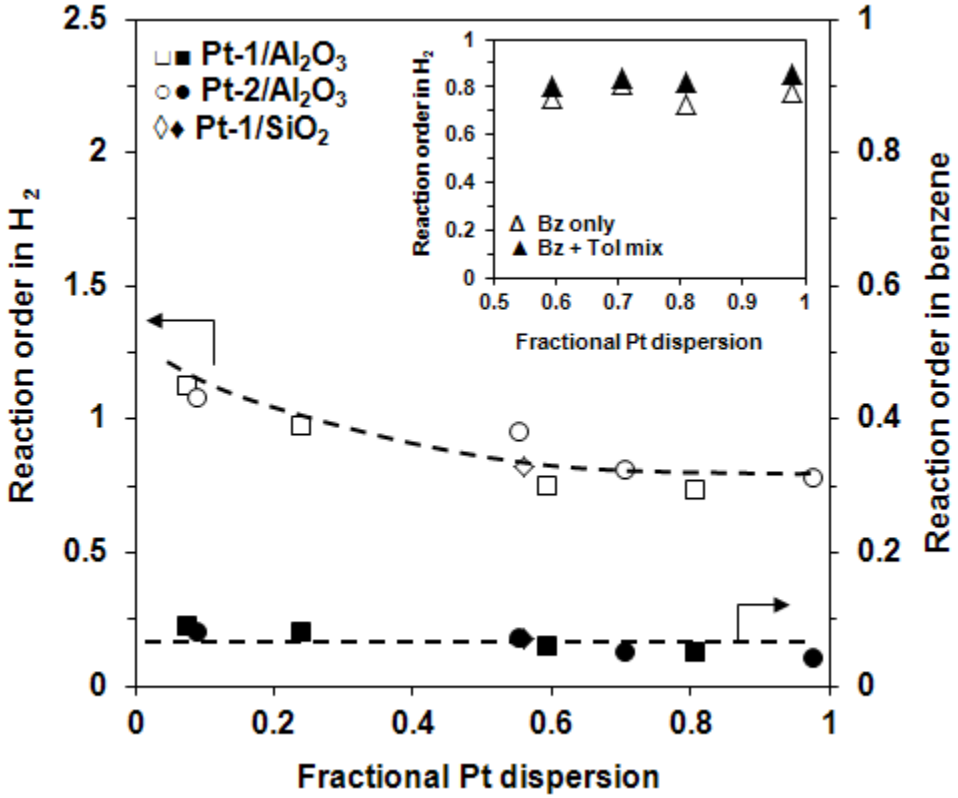

Figure S5. Effect of Pt dispersion on the reaction orders with respect to H_2 (empty symbols) and benzene (Bz, filled symbols) in benzene hydrogenation at 308 K (2−4 kPa Bz and 45−65 kPa H_2, He as balance in 101 kPa total pressure). The maximum errors in reaction orders are ± 0.01 for Bz and ± 0.04 for H_2. The inset shows that the reaction order in H_2 hardly changed when toluene (Tol) was present in 0−3.4 kPa; the reaction order in benzene also hardly changed when toluene was present (not shown).

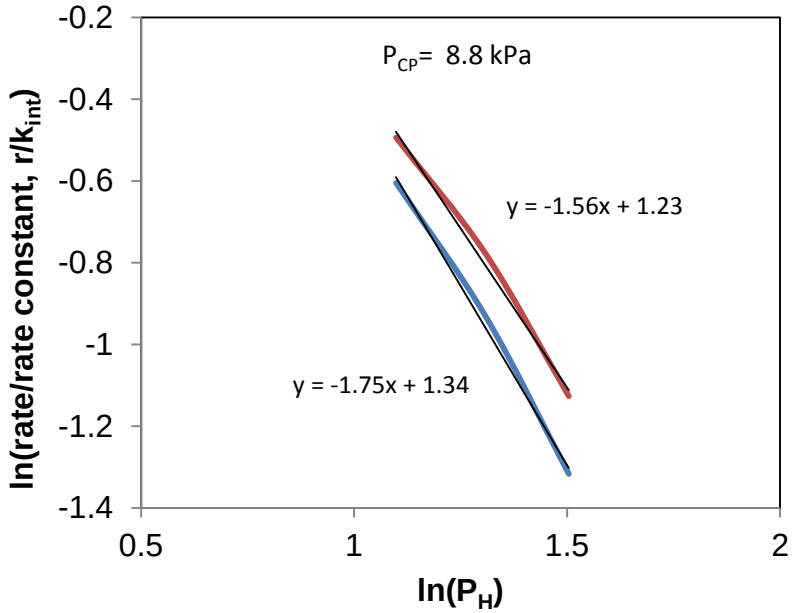

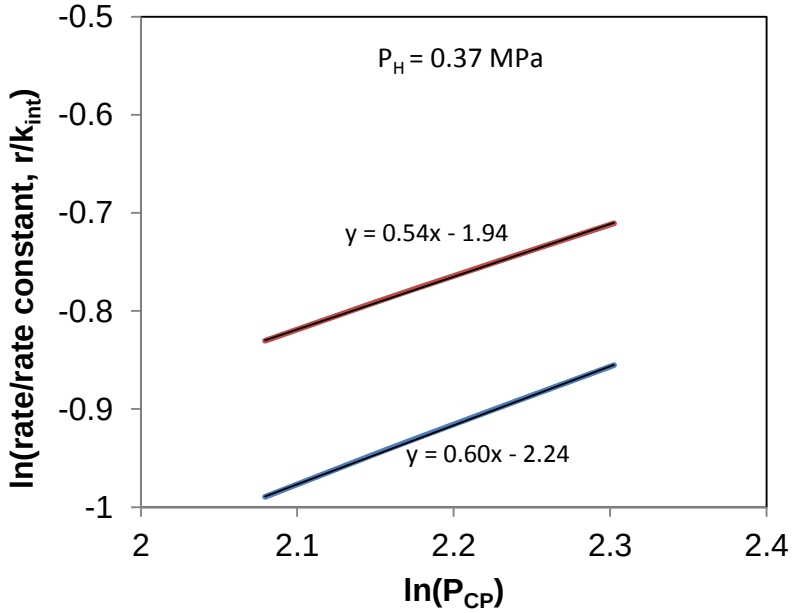

Figure S6. Predicted reaction orders in CP and H_2 show that the H-adsorption strength influences more the reaction order in H_2 (upper) than that in CP (below). The H-adsorption strength (K_H) is assumed to be 25% weaker for the red line than for the blue line.

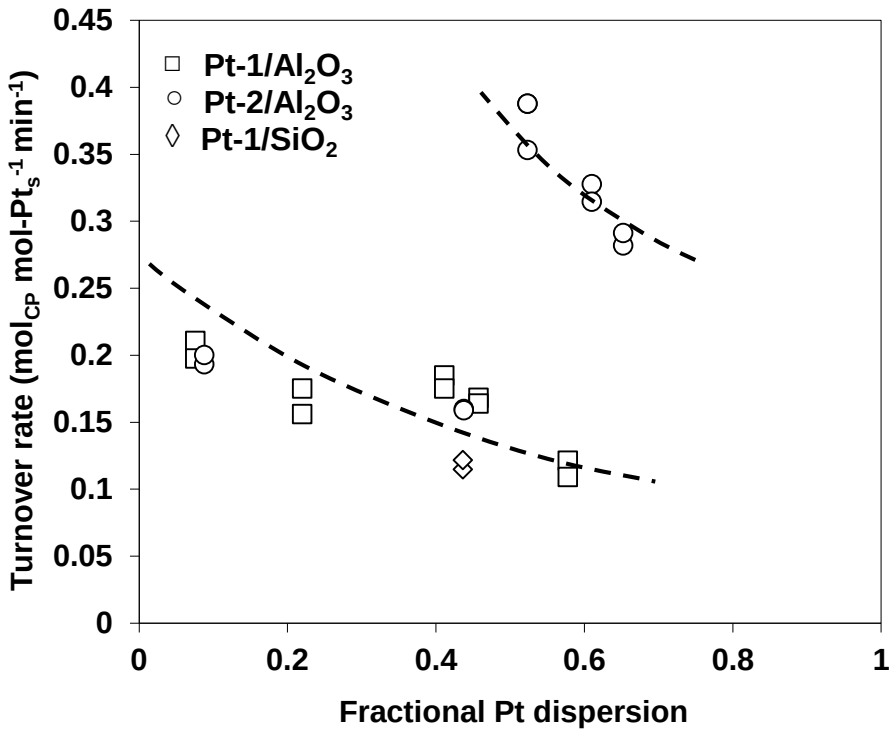

Figure S7. Surface-exposed-Pt-based rates for cyclopentane (CP) hydrogenolysis at 533 K, 8.8 kPa CP and 370 kPa H_2 as a function of Pt dispersion on Pt catalysts. Both TOF and dispersion values were calculated by assuming different H/Pt_s stoichiometries for different dispersions (see Section S4).

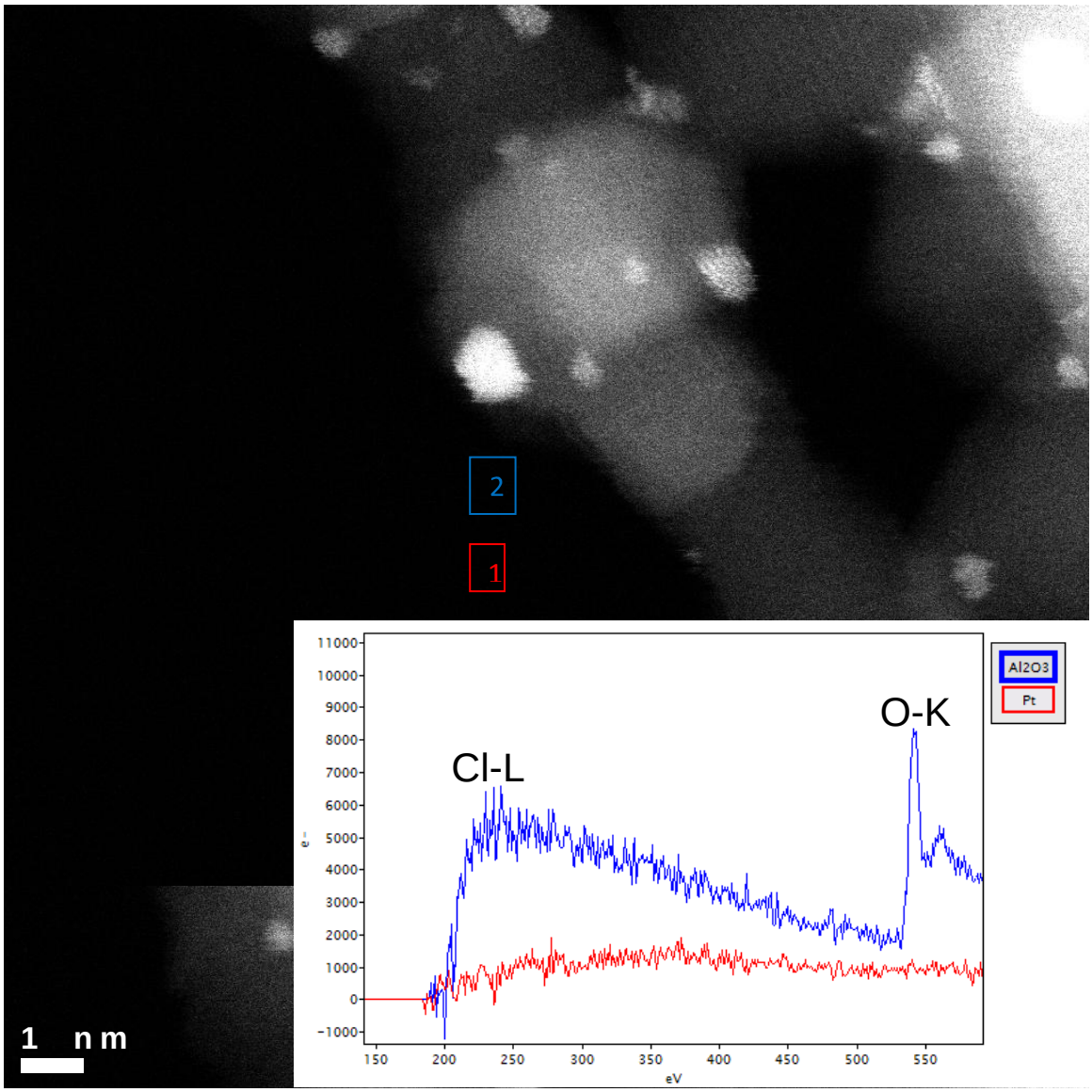

Figure S8. HAADF-STEM image of a typical high dispersion Pt/Al_2O_3 sample prepared from H_2PtCl_6 precursor. The actual diameter of the electron probe for EELS analysis is 0.1 nm. The inset shows the EELS spectra collected on area 1 and 2, which correspond to a Pt-on-top area and Al_2O_3 area, respectively. The EELS results were acquired at 300 kV accelerating voltage.

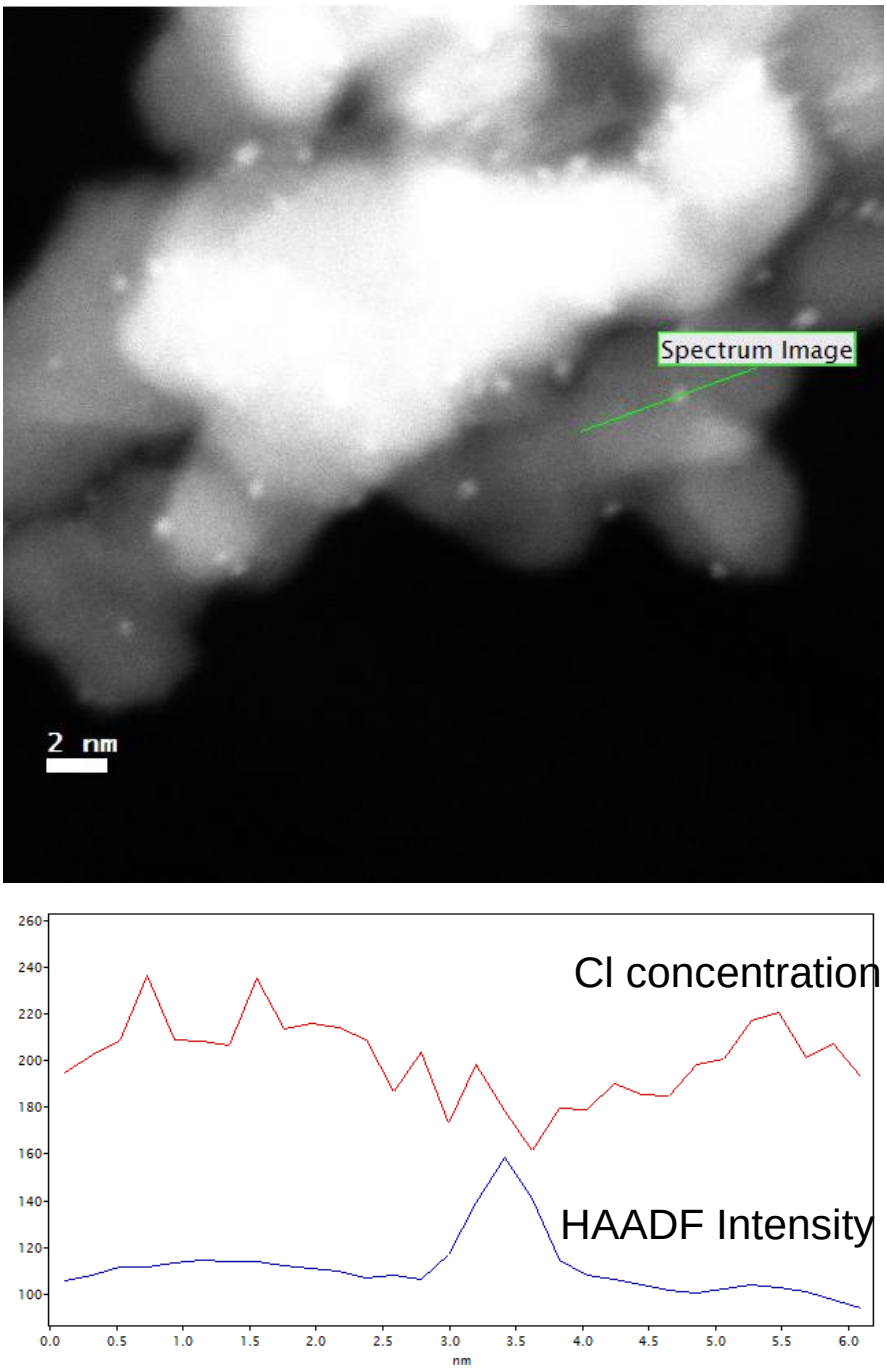

Figure S9. A typical HAADF-STEM image (upper) and EELS line-scan profile (below) of the Pt(0.98)-2/Al_2O_3 catalyst. The EELS results were acquired at 80 kV accelerating voltage.

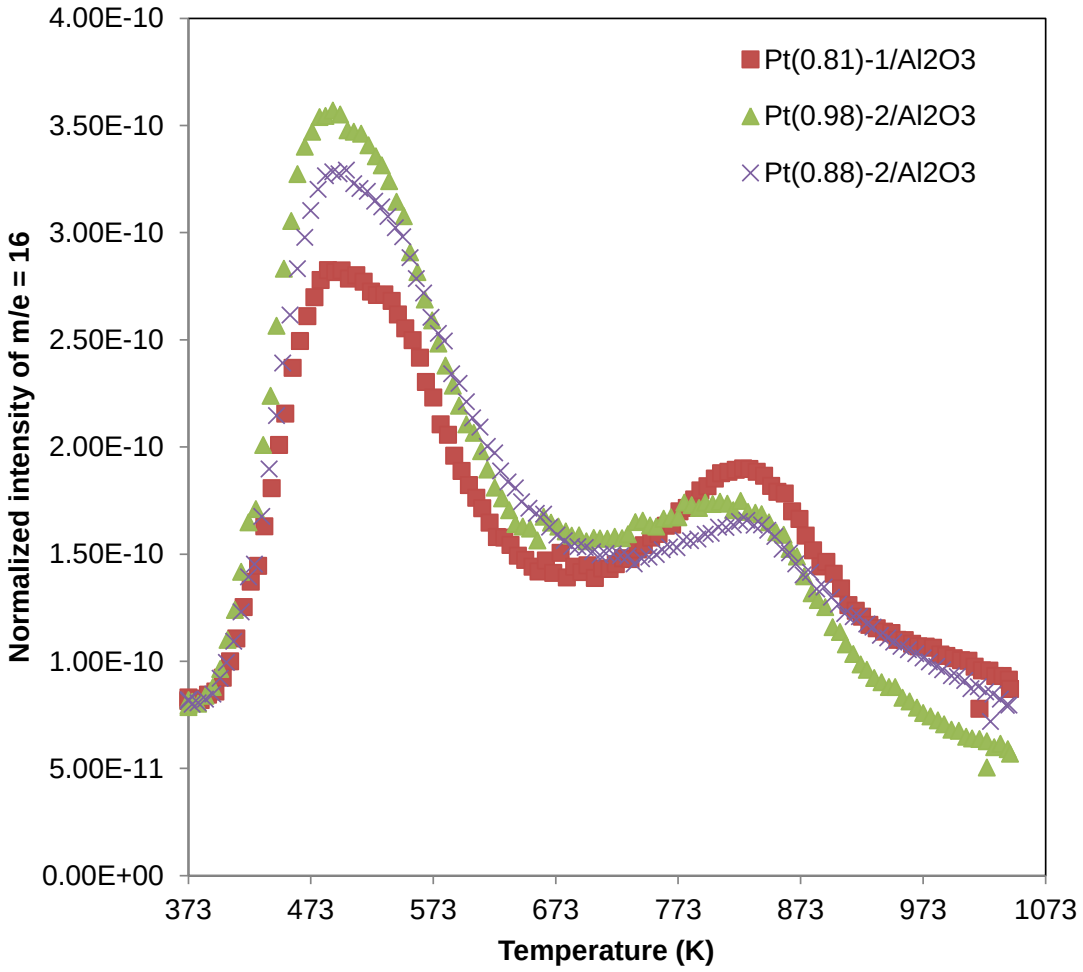

Figure S10. NH_3-TPD profiles of (■) Pt(0.81)-1/Al_2O_3, (▲) Pt(0.98)-2/Al_2O_3 and (×) Pt(0.88)-2/Al_2O_3. Signal intensities (m/e = 16) have been normalized by the sample weight.

Table S1 Turnover rates (TOR) for ring opening of cyclopentane (CP) at 533 and 553 K (8.8 kPa CP and 0.37 MPa H_2) on Cl(1%)-Al_2O_3, mechanical mixtures of Pt/SiO_2 and Cl(1%)-Al_2O_3, and Pt(0.81)-1/Al_2O_3 impregnated with 1% Cl (Cl(1%)-Pt(0.81)-1/Al_2O_3). The Cl loading (1%) is the incipient value for impregnation, in the form of NH_4Cl.[a]

Catalyst bed (mg)		TOR (mol-CP mol-Pt_s^{-1} min^{-1})	
Pt/SiO_2	Cl(1%)-Al_2O_3	T_{rxn} = 533 K	T_{rxn} = 553 K
0	40	––[b]	––[b]
20	20	0.093 ± 0.005	0.53 ± 0.02
8	30	0.091 ± 0.004	0.54 ± 0.03
40	0	0.089 ± 0.004	0.51 ± 0.02
	Cl(1%)-Pt(0.81)-1/Al_2O_3	T_{rxn} = 533 K	T_{rxn} = 553 K
	20	0.112 ± 0.007	n.m.

[a] Cl(1%)-Al_2O_3 and Cl(1%)-Pt(0.81)-1/Al_2O_3 were prepared by impregnation of NH_4Cl solution containing an incipient Cl loading of 1 wt.% (support dry weight basis), Cl(1%)-Al_2O_3 was dried at 393 K and calcined at 573 K, while Cl(1%)-Pt(0.81)-1/Al_2O_3 was, additional to the same treatments in air, reduced in H_2 at 673 K (standard settings of flow rates and durations described in the Experimental); mechanical mixtures of Cl(1%)-Al_2O_3 and Pt/SiO_2 contain both components as 180−280 μm sieved fractions.

[b] Below GC detection limit even at the lowest achievable space velocity and up to 573 K.

Table S2 Estimated population of four types of surface atoms in a cuboctahedral model for five cluster sizes (i.e. shell number m: 3, 5, 10, 20 and 40, respectively)[a]

Type	CN	Fraction of surface atoms				
		Pt_{55} (1.3 nm, D = 0.76)[b]	Pt_{309} (1.9 nm, D = 0.52)[b]	Pt_{2869} (3.5 nm, D = 0.28)[b]	Pt_{24739} (6.8 nm, D = 0.15)[b]	Pt_{205479} (13.5 nm, D = 0.074)[b]
Corner	5	0.286	0.074	0.015	0.003	0.0007
Edge	7	0.571	0.444	0.236	0.120	0.06
(100)	8	0.143	0.333	0.473	0.538	0.569
(111)	9	0	0.148	0.276	0.339	0.370

[a] Numerical formulae: N_t (number of total atoms) = $1/3(2m-1)(5m^2-5m+3)$, N_s (number of surface atoms) = $10m^2 - 20m + 12$; N_{corner} (number of corner atoms) = 12; N_{edge} (number of edge atoms) = $24(m-2)$; $N_{(100)}$ (number of (100) terrace atoms) = $6(m - 2)^2$; $N_{(111)}$ (number of (111) terrace atoms) = $4(m - 3)(m - 2)$.

[b] D (dispersion) = N_s/N_t, d (cluster size) ≈ 1.00/D.

Table S3 Estimated population of three types of surface atoms in an icosahedron model for five cluster sizes (i.e. shell number m: 3, 5, 10, 20 and 40, respectively)[a]

Type	CN	Fraction of surface atoms				
		Pt_{55} (1.3 nm, D = 0.76)[b]	Pt_{309} (1.9 nm, D = 0.52)[b]	Pt_{2869} (3.5 nm, D = 0.28)[b]	Pt_{24739} (6.8 nm, D = 0.15)[b]	Pt_{205479} (13.5 nm, D = 0.074)[b]
Corner	6	0.286	0.074	0.015	0.003	0.0007
Edge	8	0.714	0.556	0.296	0.150	0.075
(111)	9	0	0.370	0.689	0.847	0.924

[a] Numerical formulae: N_t (number of total atoms) = $1/3(2m-1)(5m^2-5m+3)$, N_s (number of surface atoms) = $10m^2 - 20m + 12$; N_{corner} (number of corner atoms) = 12; N_{edge} (number of edge atoms) = 30(m-2);; $N_{(111)}$ (number of (111) terrace atoms) = $10(m - 3)(m - 2)$.

[b] D (dispersion) = N_s/N_t, d (cluster size) ≈ 1.00/D.